Estimation of Compton Imager Using Single 3D Position-Sensitive LYSO Scintillator: Monte Carlo Simulation

Taewoong LEE

Health Science Research Center, Korea University, Seoul 02841, Korea

Hyounggun LEE and Younghak KIM

Department of Bio-Convergence Engineering, Korea University, Seoul 02841, Korea

Wonho LEE*

School of Health and Environmental Science, Korea University, Seoul 02841, Korea

The performance of a Compton imager using a single three-dimensional position-sensitive LYSO scintillator detector was estimated using a Monte Carlo simulation. The Compton imager consisted of a single LYSO scintillator with a pixelized structure. The size of the scintillator and each pixel were $1.3 \times 1.3 \times 1.3$ cm^3 and $0.3 \times 0.3 \times 0.3$ cm^3, respectively. The order of γ-ray interactions was determined based on the deposited energies in each detector. After the determination of the interaction sequence, various types of reconstruction algorithms such as simple back-projection, filtered back-projection, and list-mode maximum-likelihood expectation maximization (LM-MLEM) were applied and compared with each other in terms of their angular resolution and signal-to-noise ratio (SNR) for several γ-ray energies. The LM-MLEM reconstruction algorithm exhibited the best performance for Compton imaging in maintaining high angular resolution and SNR. The two sources of ^{137}Cs (662 keV) could be distinguishable if they were more than 17° apart. The reconstructed Compton images showed the precise position and distribution of various radiation isotopes, which demonstrated the feasibility of the monitoring of nuclear materials in homeland security and radioactive waste management applications.

I. INTRODUCTION

The Compton imaging technique uses sequential γ-ray interactions in a single detector or multiple detectors [1–3]. When a photon undergoes effective Compton scattering in detectors, the cosine angle of the photon scattering can be calculated to reconstruct the source distribution based on the position and energy of the interactions in the detectors [1–3]. With a three-dimensional (3D) position-sensitive technique, cadmium zinc telluride (CZT) semiconductor detectors have been widely used as an alternative for room-temperature operation with good position and energy resolution. A Compton camera consisting of two CZT detectors that are 3D position-sensitive was developed by Du *et al.* in 2001 [4]. In 2004, Lehner *et al.* demonstrated 4π Compton imaging using a single 3D position-sensitive CZT detector that

could measure the 3D position of interactions, and they proposed a weighted list-mode maximum likelihood algorithm for Compton imaging [5]. Xu *et al.* showed the performance of a Compton imager of various reconstruction algorithms using single 3D position-sensitive CZT detectors [6]. To construct the Compton camera of a large-volume mosaic array, Lee *et al.* developed a Compton camera consisting of CZT crystals with Frisch-grid detectors and showed promising results for the Compton imaging of three different radiation isotopes [7].

In recent years, the "dual-sided" read-out of scintillation crystal arrays has been developed [8,9]. The scintillation light signals of cubic structure scintillation crystal arrays can be read out by using multi-pixel photon counters (MPPCs) coupled at both ends of a scintillator crystal block, and the depth information (Z-direction) can be calculated using the pulse height ratio from the top and bottom of the MPPCs [8,9]. Hence, the scintillation detector of a cubic structure can provide the 3D information. Kataoka *et al.* developed a Compton imager con-
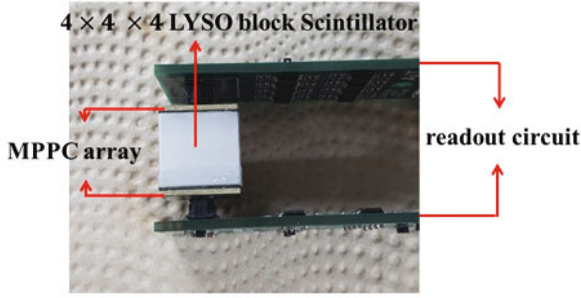
*E-mail: wonhol@korea.ac.kr; Fax: +82-2-940-2829

Fig. 1. (Color online) Photograph of the detection system with electrodes.

Fig. 2. (Color online) Schematic diagram of a 3D position-sensitive $4 \times 4 \times 4$ block array of LYSO scintillator Compton camera.

sisting of two cubic crystal array detectors of GAGG:Ce scintillator with 3D position sensitivity in 2013 [10]. In 2014, Takeuchi *et al.* developed a stereo Compton camera and demonstrated the 3D localization of radioisotopes by using the triangulation surveying method [11].

In this study, we designed a Compton camera based on a single 3D position-sensitive LYSO scintillator detector. The Compton imaging with various reconstruction algorithms was simulated by using the Monte Carlo method and was compared in terms of their angular resolutions and signal-to-noise ratios (SNRs). The deposited energies of the γ-ray interactions in the detectors were utilized to determine the correct sequential order of the interactions. Under the correct sequential order, the performance of the reconstructed Compton image was evaluated according to the incident radiation energies and algorithms. Our research is focused on the feasibility of a portable imager in monitoring nuclear materials in homeland security and radioactive waste management applications.

II. MATERIALS AND METHODS

1. Geometrical Structure and Interaction Sequence

Figure 1 shows the Compton detection system, which is based on an MPPC array (Model: S12314, Hamamatsu, Japan) of 4×4 channels coupled to both ends of real single 3D position-sensitive LYSO scintillator blocks. The LYSO scintillators with a density of 7.1 g/cm^3, made by Siccas, consists of $4 \times 4 \times 4$ pixels whose size is $3 \times 3 \times 3$ mm^3 each. The whole size of the detection system is only about $1.3 \times 1.3 \times 1.2$ cm^3.

The schematic diagram and configuration of the simulation setup are illustrated in Fig. 2. For the Compton imaging, the point sources ^{133}Ba (356 keV), ^{137}Cs (662 keV), and ^{22}Na(1275 keV) with an activity of 20 μCi are located 15 cm away from the top of the detector array, and the measurement time is 600 s. The total amount of radiations emitted from a source was 444 million. When
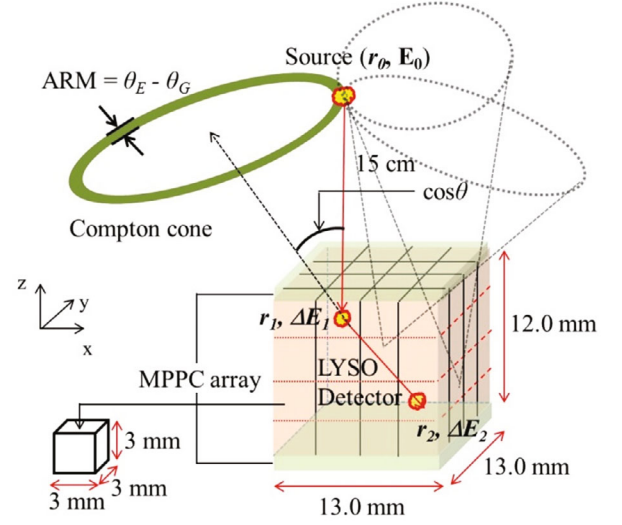
the incident radiation is the scattered in first interaction and absorbed in the second interaction, the positions (r_1, r_2) and energy information $(\Delta E_1, \Delta E_2)$ can be obtained from the events of the effective Compton scattering, as shown in Fig. 2. In a real detection system, the interaction of the z-direction (depth information) can be estimated using the following centroid equation [9]:

$$Z = \frac{LM_1}{M_1 + M_2}, \tag{1}$$

where M_1 and M_2 represent the total signal recorded for the top and bottom MPPC array, respectively. L is the depth direction length of the scintillator array. The timing resolution of the currently available effective Compton events was approximately 250 ns in the detection system. As the accidental coincidence rate was $2\tau r^2$ (τ: resolving time, r: count rate) [12], even if the background count rate was 10^4 cps, the accidental coincidence was low (49 cps). Therefore, the system can be used in high-background environments. The accidental coincidence rate is presented in Fig. 3 based on the timing resolution of the detection system.

An incorrect choice of interaction sequence can give erroneous information. Therefore, the sequential order of radiation interaction in the detectors should be correctly estimated. This method was suggested based on the assumption that a higher correct sequence count guarantees a better reconstructed Compton image [13]. As shown in Fig. 4, if the energy of the incident radiation energy is higher than 400 keV, a higher energy will be deposited in the first interaction ($E_1 > E_2$). If the radiation energy is lower than 400 keV, it is more probable that the first interaction will deposit less energy than the second interaction ($E_1 < E_2$).

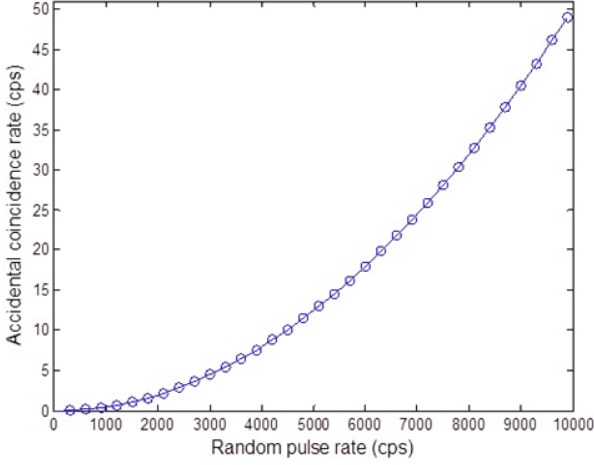A simulation code, the Geant4 Application for Tomo-

Fig. 3. (Color online) Accidental coincidence rate vs. random pulse rate for LYSO scintillator in Compton camera.
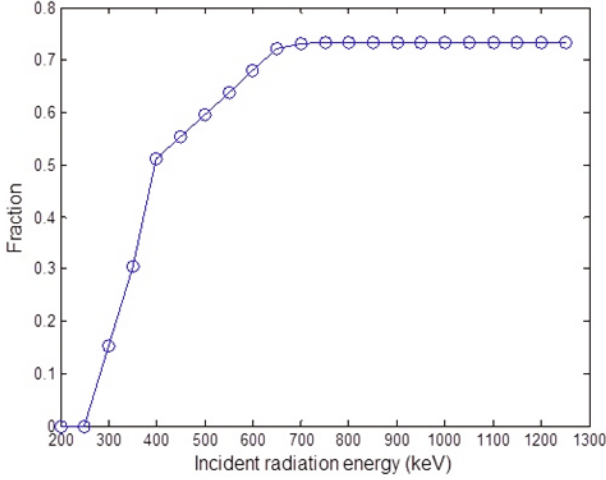

Fig. 4. (Color online) Fraction of simulated Compton events in which the first interaction deposits more energy than the second interaction.

graphic Emission (GATE 7.0), was used for the Monte Carlo calculations, and the effective Compton scattering events from the output were extracted by MATLAB2010 for image reconstruction. A 2.8 GHz CPU in a personal computer (Pentium 4) and MATLAB2010 were used to reconstruct the source image. The uncertainty factors of Doppler broadening, finite position (pixelization effect), and detector energy resolution were used.

2. Simple Back-Projection

The simple back-projection (SBP) method is a general Compton reconstruction algorithm. As shown in Fig. 2, the cosine values of the scattering angle and ARM can be determined as

$$\cos\theta_E = 1 - \frac{m_0 c^2 \Delta E_1}{E_0 \Delta E_2}, \tag{2}$$

$$\cos\theta_G = \frac{(\bar{r}_1 \cdot \bar{r}_2)}{|\bar{r}_1||\bar{r}_2|}, \tag{3}$$

$$\mathrm{ARM} = \theta_E - \theta_G, \tag{4}$$

where $m_0 c^2$ is the rest mass of the electron and $\cos\theta_E$ is the scattering angle calculated based on the deposited energy $(\Delta E_1, \Delta E_2)$ in the detectors. $\cos\theta_G$ is calculated based on the measured interaction position (r_1, r_2) and each pixel position on the source plane. $\bar{r}_1$ and $\bar{r}_2$ are the vectors from r_0 to r_1 and r_1 to r_2, respectively. By equalizing Eqs. (2) and (3), the position of the source (r_0) can be reconstructed by the back-projection of the Compton cone and the intersections of the back-projections represent the estimated source distribution.

3. Filtered Back-Projection

The Compton image reconstructed by SBP is usually blurred because the cones overlap with each other. In order to reduce the blurring in the Compton image, analytical reconstruction methods such as filtered back-projection (FBP) was developed [14,15]. The FBP algorithm for Compton imaging applications was proposed by Parra [14]. As described by Eqs. (5) and (6), the image of the FBP, $g(\Omega)$, can be performed by deconvolution which was applied for the point spread function (PSF) of an image of the SBP, $g'(\Omega')$.

$$g'(\Omega') = \int d\Omega g(\Omega) h_{bp}(\cos\omega), \tag{5}$$

$$g(\Omega) = \int d\Omega' g'(\Omega') h^{-1}(\cos\omega), \tag{6}$$

where ω is the difference between the angle calculated based on the measured direction Ω and the direction Ω' forming a SBP image $g'(\Omega')$. The convolution kernel $h_{bp}(\cos\omega)$ was derived by Parra [14]. The deconvolution kernel ($h^{-1}(\cos\omega)$) can be obtained as follow [14]:

$$h^{-1}(\cos\omega) = \sum_{n=1}^{\infty} \left(\frac{2n+1}{4\pi}\right) \frac{P_n(\cos\omega)}{H_n}, \tag{7}$$

where $P_n(\cos\omega)$ are the cosine angles with Legendre polynomials, and H_n are the coefficients of $h_{bp}(\cos\omega)$, which is the expansion of the Legendre polynomial:

$$H_n = \frac{2n+1}{2} \int d(\cos\omega) h_{bp}(\cos\omega) P_n(\cos\omega). \tag{8}$$

Figure 5(a) displays the PSF that is defined by the Klein-Nishina formula. The coefficient H_n converges to a constant value rather than zero when the n-value is large, as shown in Fig. 5(b).
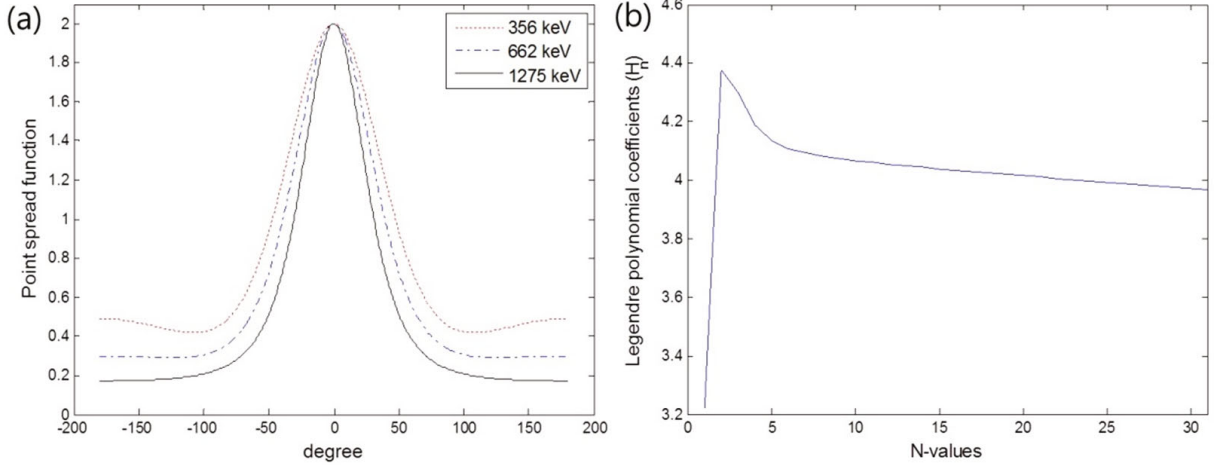
Fig. 5. (Color online) (a) PSF with various energies and (b) expansion coefficients in the base of the Legendre polynomial at 662 keV.

4. List-Mode MLEM

The expectation maximization (EM) is an iterative algorithm that determines the maximum likelihood (ML) [16]. Hence, the MLEM algorithm, including the Poisson distribution, were widely used in the Compton imaging to precisely reconstruct the source distribution for the limited amount of measured data. The source distribution can be estimated as follows:

$$\lambda_j^{n+1} = \frac{\lambda_j^n}{\sum_i t_{ij}} \sum_i \frac{t_{ij} Y_i}{\sum_k t_{ik} \lambda_k^n}, \tag{9}$$

where λ_j^{n+1} and λ_j^n are the estimated values of a source pixel j after the $(n+1)$-th and n-th iteration. Y_i is the measured number of counts in a detector event i. In general, in the MLEM algorithm, the system matrix (t_{ij}), including the total number of possible combinations of Compton imaging, can be extremely large, which requires a long calculation time. To reduce the calculation time, we applied a list-mode MLEM (LM-MLEM). In the LM- MLEM case, Y_i is unity ($=1$) for all measured events because the total number of photons detected is significantly smaller than the number of possible combinations of position and energy measurements [7]. Hence the matrix size for the image processing dramatically decreases, and the calculation time also decreases. The analytical system matrix for the LM-MLEM of Compton imaging was proposed by Wilderman *et al.* [17]. The t_{ij} is the analytical system matrix, which includes the probabilities of all the interactions of Compton events in the detection system. The t_{ij} can be obtained as follows:

$$t_{ij} = \exp(-\mu_t(E_0)D_1) \times KN \times \exp(-\mu_t(E_2)D_2), \tag{10}$$

where $\mu_t(E_0)$, and $\mu_t(E_2)$ are the total attenuation coefficients at the initial and scattered energies, E_0 and E_2, respectively. D_1 is the attenuation distance between the source plane and first interaction position, D_2 is the

attenuation distance between the first and second interaction positions, and KN is the differential Compton cross -section (Klein-Nishina formula).

III. RESULTS

After the correct sequential order was chosen, the performance of the reconstructed Compton image from various reconstruction algorithms and several γ-ray energies was evaluated based on a Monte Carlo simulation. The Compton images reconstructed using SBP, FBP, and LM-MLEM for 356, 662, and 1275 keV point sources are presented in Figs. 6 - 8.

As expected, the Compton images reconstructed using LM-MLEM are sharper and have fewer artifacts than those using the SBP and FBP algorithms. The quality of the Compton images improves with the increase in incident energy because the energy uncertainty and Doppler broadening are inversely proportional to radiation energy [18]. The width of each back-projection cone for Compton imaging was set based on that of the angular resolution measure (ARM). The ARM is the difference between the angles calculated based on the position and energy information (*cf.* Eq. (4)). The full-width half-maximum (FWHM) of the ARM for 356, 662, and 1275 keV are 32.3, 22.8, and 9.98°, respectively.

Figures 9 - 10 show the quantitative evaluation of the Compton images using the angular resolution and SNRs. The angular resolution is represented by the FWHM of the point source, and the SNR can be calculated by using the following equation:

$$\text{SNR} = \frac{\bar{s}}{\sqrt{\frac{\sum (x_i - \bar{x})^2}{n}}}, \tag{11}$$

where $\bar{s}$ is the average value of the source pixels including the maximum pixel, x_i and $\bar{x}$ are the value of each
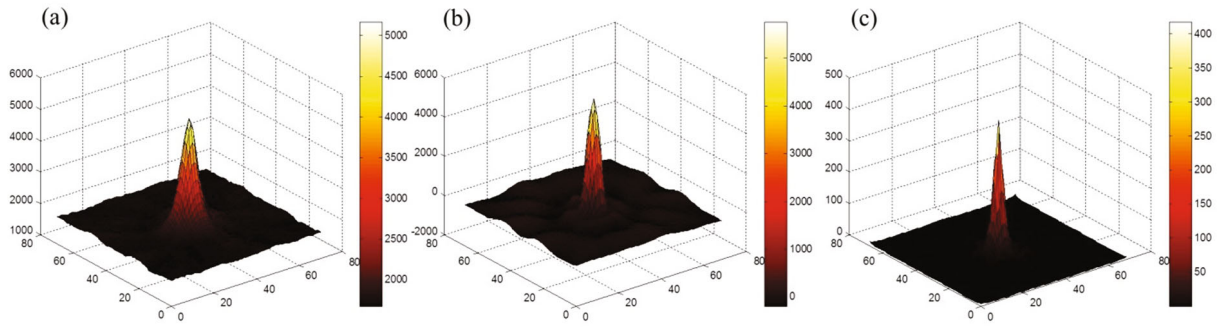
Fig. 6. (Color online) Reconstructed image using various reconstruction algorithms for a 356 keV point source: (a) SBP, (b) FBP, and (c) LM-MLEM.
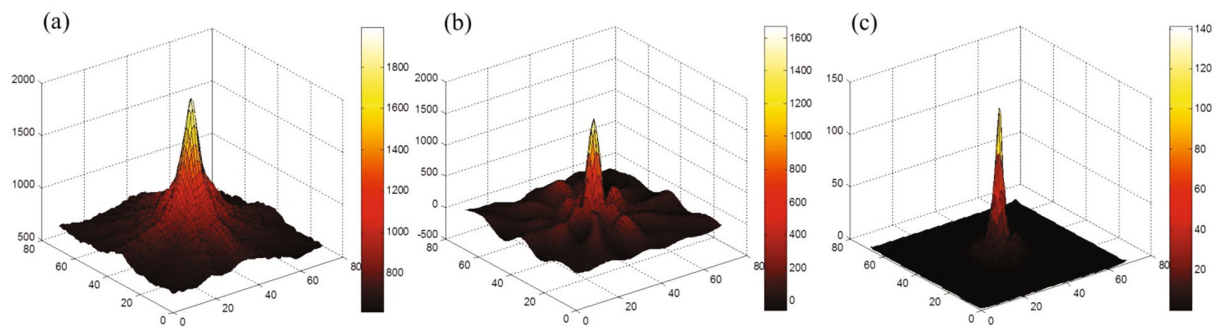

Fig. 7. (Color online) Reconstructed image using various reconstruction algorithms for a 662 keV point source: (a) SBP, (b) FBP, and (c) LM-MLEM.
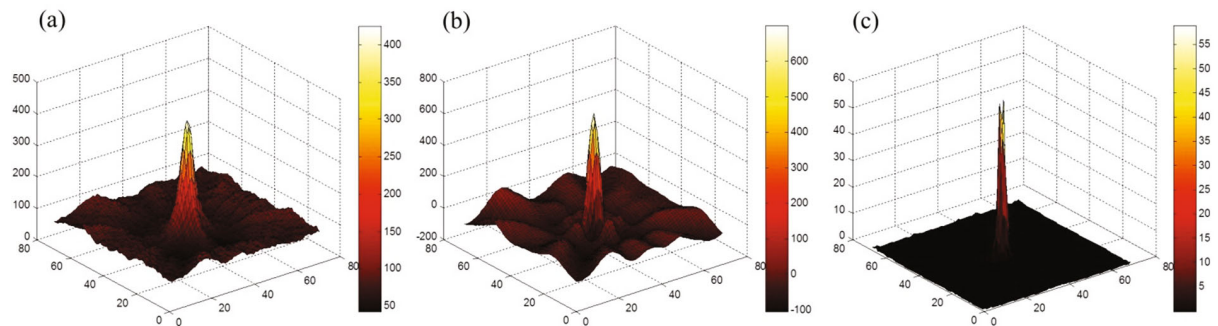

Fig. 8. (Color online) Reconstructed image using various reconstruction algorithms for a 1275 keV point source: (a) SBP, (b) FBP, and (c) LM-MLEM.
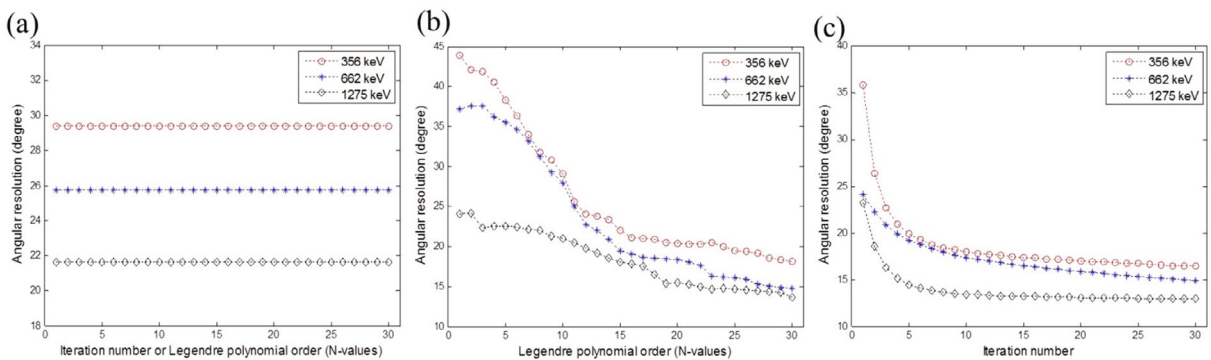

Fig. 9. (Color online) Angular resolution of the Compton imager for various reconstruction algorithms: (a) SBP, (b) FBP, and (c) LM-MLEM.
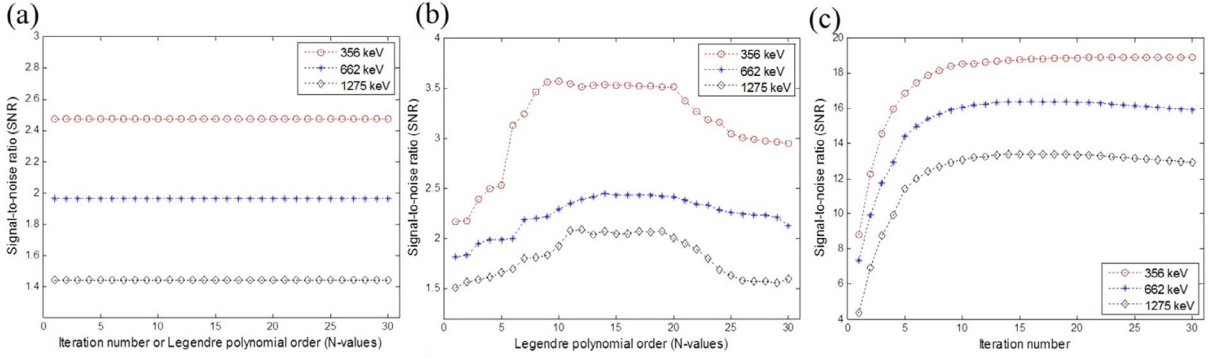
Fig. 10. (Color online) SNR of the Compton imager for various reconstruction algorithms: (a) SBP, (b) FBP, and (c) LM-MLEM.
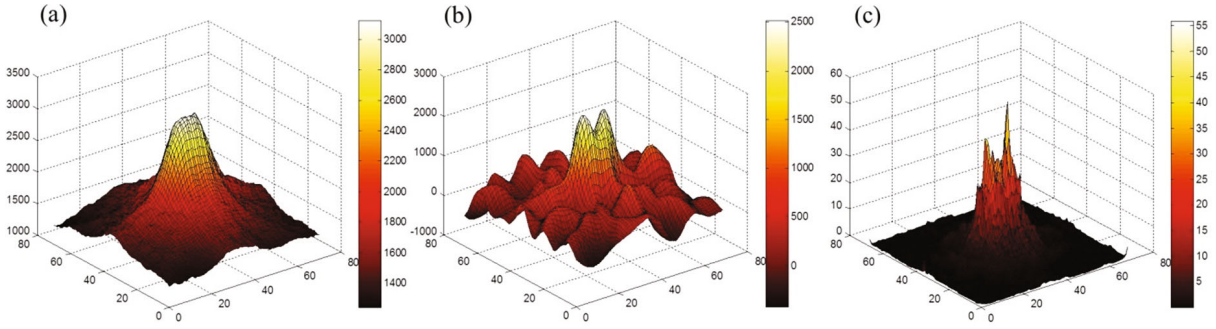

Fig. 11. (Color online) Compton imagers of two ^{137}Cs (662 keV) point sources placed 17° apart: (a) SBP, (b) FBP (*n*-value = 25), and (c) LM-MLEM (iteration = 25).

pixel excluding source pixels and the average of x_i, respectively, n is the number of pixels x_i. The absolute efficiency is defined by

$$\text{Absolute efficiency} = \frac{N_r}{N_i}, \qquad (12)$$

where N_r is the effective count used for the reconstructed Compton image, and N_i is the total number of photons emitted by the source (20 μCi).

The performance of the angular resolution, as explained above, improves with the increase in incident radiation energy, and the angular resolution of the FBP and LM-MLEM improves with the *n*-values and number of iterations, as shown in Fig. 9. The angular resolution of the SBP is constant, regardless of the number of iterations or *n*-value. The SBP algorithm is equivalent to the FBP at the approximately 10th Legendre polynomial order because only low-frequency components in the FBP reconstructed images are calculated at low *n*-values; hence, the image reconstructed using the FBP with a low *n*-value is blurred.

As shown in Fig. 10, the performance of the SNR decreases with the increasing incident γ-ray energy, which is mainly due to the decrease in detection efficiency caused by the increase in radiation penetration with incident γ-ray energy. The SNR of the SBP exhibits a constant value, regardless of the number of iterations or *n*-value. The SNR of the FBP and LM-MLEM increases

with the *n*-value and number of iterations, but only before reaching saturation at the approximately 10th-15th point. The reconstructed Compton image obtained using LM-MLEM has a higher SNR than those obtained using the SBP and FBP reconstruction algorithms.

Table 1 summarizes the detection efficiency, ARM, angular resolution, and SNR for each radiation source from various reconstruction algorithms. The angular resolution and SNR of the reconstructed Compton images using the LM-MLEM algorithm show the best performance (*cf.* Figs. 9, 10, and Table 1).

To evaluate the resolution limit of the reconstructed Compton images, two point ^{137}Cs sources (662 keV) of equal activity (20 μCi) with varying separations were used. The measurement time and size of each image pixel were 600 s and 5 mm, respectively. When the angular distance between the two point sources was greater than 17°, the sources could be distinguishable, as shown in Fig. 11. However, the SBP algorithm could not distinguish between the two sources, and the reconstructed Compton image using the LM-MLEM algorithm exhibited the least noise and fewest artifacts among the three algorithms.

Table 1. Results achieved by a various image reconstruction algorithms.

Energy (keV)	Absolute efficiency	ARM	Reconstruction algorithms	Angular resolution (°)	SNR
356	5.01×10^{-5}	32.3°	SBP	29.3	2.47
			FBP (n-value = 15)	23.3	3.52
			LM-MLEM (iteration = 15)	17.6	18.76
662	1.81×10^{-5}	22.8°	SBP	25.7	1.96
			FBP (n-value = 15)	20.9	2.43
			LM-MLEM (iteration = 15)	16.4	16.38
1275	2.44×10^{-6}	9.98°	SBP	21.6	1.44
			FBP (n-value = 15)	19.1	2.05
			LM-MLEM (iteration = 15)	13.23	13.38

IV. CONCLUSION

By using a voxel array of LYSO scintillator detectors, we designed a compact Compton camera and estimated the performance of the Compton imager with an effective assumption of the γ-ray interaction sequence and three types of reconstruction algorithms. In the simulation results, both the angular resolution and SNR of the images reconstructed by the LM-MLEM algorithm were better than those of the SBP and FBP algorithms. The two point sources could be distinguished from each other if the angular distance was over 17°. The results of our simulation demonstrated the feasibility of using a voxel array of LYSO scintillator detectors to monitor several γ-ray energies in the investigation of nuclear materials. An experimental setup with the design presented in this paper and an applied imaging technique will be examined in a future study.

ACKNOWLEDGMENTS

REFERENCES

[1] M. Singh and D. Doria, Med. Phys. **10**, 421 (1983).
[2] M. Singh and D. Doria, Med. Phys. **10**, 428 (1983).
[3] M-H. Richard, M. Chevallier, D. Dauvergne, N. Freud, P. Henriqet, F. Le Foulher, J. M. Lètang, G. Montarou, C. Ray, F. Roellinghoff, E. Testa and A. H. Walenta, IEEE Trans. Nucl. Sci. **58**, 87 (2011).
[4] Y. F. Du, Z. He, G. F. Knoll, D. K. Wehe and W. Li, Nucl. Instrum. Meth. A **457**, 203 (2001).
[5] C. E. Lehner, Z. He and F. Zhang, IEEE Trans. Nucl. Sci. **51**, 1618 (2004).
[6] D. Xu, Z. He, C. E. Lehner and F. Zhang, Proc. SPIE. **5540**, 144 (2004).
[7] W. Lee, A. Bolotnikov, T. Lee, G. Camarda, Y. Cui, R. Gul, A. Hossain, R. Utpal, G. Yang and R. James, IEEE Trans. Nucl. Sci. **63**, 259 (2016).
[8] E. Yoshida, Y. Hirano, H. Tashima, N. Inadama, F. Nishikido, T. Moriya, T. Omura, M. Watanabe, H. Murayama and T. Yamaya, Nucl. Instrum. Meth. A **723**, 83 (2013).
[9] A. Kishimoto, J. Kataoka, T. Kato, T. Miura, T. Nakamori, K. Kamada, S. Nakamura, K. Sato, Y. Ishikawa, K. Yamamura, N. Kawabata and S. Yamamoto, IEEE Trans. Nucl. Sci. **60**, 38 (2013).
[10] J. Kataoka, A. Kishimoto, T. Nishiyama, T. Fujita, K. Takeuchi, T. Kato, T. Nakamori, S. Ohsuka, S. Nakamura, M. Hirayanagi, S. Adachi, T. Uchiyama and K. Yamamoto, Nucl. Instrum. Meth. A **732**, 403 (2013).
[11] K. Takeuchi, J. Kataoka, T. Nishiyama, T. Fujita, A. Kishimoto, S. Ohsuka, S. Nakamura, S. Adachi, M. Hirayanagi, T. Uchiyama, Y. Ishikawa and T. Kato, Nucl. Instrum. Meth. A **765**, 187 (2014).
[12] G. F. Knoll, *Radiation Detection and Measurement*, 4th ed. (Wiley, New York, 2010), Chap. 10, p. 336.
[13] Y. F. Du, Z. He, G. F. Knoll and D. K. Wehe, W. Li, Nucl. Instrum. Meth. A **457**, 203 (2001).
[14] L. C. Parra, IEEE Trans. Nucl. Sci. **47**, 1543 (2000).
[15] D. Xu and Z. He, IEEE Trans. Nucl. Sci. **53**, 2787 (2006).
[16] K. Lange and R. Carson, J. Comput. Assist. Tomogr. **8**, 306 (1984).
[17] S. J. Wilderman, N. H. Clinthorne, J. A. Fessler and W. L. Rogers, Proc. IEEE Nucl. Sci. Symp. Conf. Rec. **3**, 1716 (1998).
[18] Y. F. Yang, Y. Gono, S. Motomura, S. Enomoto and Y. Yano, IEEE Trans. Nucl. Sci. **48**, 656 (2001).